The Emerald Research Register for this journal is available at
www.emeraldinsight.com/researchregister

The current issue and full text archive of this journal is available at
www.emeraldinsight.com/0961-5539.htm

Received February 2004
Revised October 2004
Accepted October 2004

Three-dimensional numerical simulation of *g*-jitter induced convection and solute transport in magnetic fields

K. Li, B.Q. Li and J. Handa
School of Mechanical and Materials Engineering, Washington State University, Pullman, Washington, USA, and
H.C. de Groh
NASA Glenn Research Center, Cleveland, Ohio, USA

Abstract

Purpose – The quality of crystals grown in space can be diversely affected by the melt flows induced by *g*-jitter associated with a space vehicle. This paper presents a full three-dimensional (3D) transient finite element analysis of the complex fluid flow and heat and mass transfer phenomena in a simplified Bridgman crystal growth configuration under the influence of *g*-jitter perturbations and magnetic fields.

Design/methodology/approach – The model development is based on the Galerkin finite element solution of the magnetohydrodynamic governing equations describing the thermal convection and heat and mass transfer in the melt. A physics-based re-numbering algorithm is used to make the formidable 3D simulations computationally feasible. Simulations are made using steady microgravity, synthetic and real *g*-jitter data taken during a space flight.

Findings – Numerical results show that *g*-jitter drives a complex, 3D, time dependent thermal convection and that velocity spikes in response to real *g*-jitter disturbances in space flights, resulting in irregular solute concentration distributions. An applied magnetic field provides an effective means to suppress the deleterious convection effects caused by *g*-jitter. Based on the simulations with applied magnetic fields of various strengths and orientations, the magnetic field aligned with the thermal gradient provides an optimal damping effect, and the stronger magnetic field is more effective in suppressing the *g*-jitter induced convection. While the convective flows and solute transport are complex and truly 3D, those in the symmetry plane parallel to the direction of *g*-jitter are essentially two-dimensional (2D), which may be approximated well by the widely used 2D models.

Originality/value – The physics-based re-numbering algorithm has made possible the large scale finite element computations for 3D *g*-jitter flows in a magnetic field. The results indicate that an applied magnetic field can be effective in suppressing the *g*-jitter driven flows and thus enhance the quality of crystals grown in space.

Paper type Research paper

Keywords Simulation, Crystal growth, Fluid flow, Heat transfer, Magnetic fields

International Journal of Numerical Methods for Heat & Fluid Flow
Vol. 15 No. 8, 2005
pp. 872-893
© Emerald Group Publishing Limited
0961-5539
DOI 10.1108/09615530510625138

Financial support of this work by NASA Microgravity Division (Grant Nos: NCC8-92 and NAG8-1693) is gratefully acknowledged, and so is Cindy Zhang's assistance in developing the 3D computer graphics capabilities used in the paper.

Nomenclature

B_0 = applied magnetic field magnitude
$\mathbf{B}$ = applied magnetic field
C_p = heat capacity of melt
C = concentration
$\mathbf{C}$ = discretized concentration vector
$\mathbf{C_B}$ = the buoyancy matrix
$\mathbf{C_p}$ = the gradient matrix
d = cylinder diameter
D = diffusion coefficient of solute
f = g-jitter perturbation frequency
$\mathbf{F_U}$ = force vector
g = g-jitter perturbation magnitude
g_0 = earth gravity ($9.8\,\mathrm{m\,s^{-2}}$)
$\mathbf{g}$ = gravity vector
$\mathbf{g}^*$ = gravity unity vector
Ha = Hartman number ($Ha = BL\sqrt{\sigma/\mu}$)
$\hat{i},\hat{j}$ = unit vectors of the ith, jth component
k = solutal segregation coefficient
$\mathbf{K}$ = diffusion matrix
L = length
L_0 = length scale
$\mathbf{M}$ = mass matrix
$\mathbf{n}$ = the outward normal
$\mathbf{N}$ = advection matrix
p = pressure
P_0 = pressure scale
Pr = Prandtl number ($Pr = \nu/\alpha$)
$\mathbf{P}$ = discretized nodal pressure vector
Ra = Rayleigh number ($Ra(t) = \beta g(t)(T_\mathrm{h} - T_\mathrm{m})L^3/\nu\alpha$)
Sc = Schmidt number ($Sc = \nu/D$)
t = time
t_0 = time scale
T = temperature
$T = (\theta^* - T_\mathrm{m})/(T_\mathrm{h} - T_\mathrm{m})$
T_m = dimensional melting temperature
T_h = dimensional temperature at inlet
$\mathbf{T}$ = discretized temperature vector
U_0 = velocity scale
$\mathbf{u}$ = velocity vector
$\hat{\boldsymbol{u}}$ = unit velocity vector
$\mathbf{U}$ = discretized velocity vector
V_m = heater translation velocity
x,y,z = dimensionless coordinates

Greek

κ = thermal diffusivity
β = thermal expansion coefficient
δ_{ij} = delta function
μ = dynamic viscosity
ν = kinematic viscosity
θ^* = dimensional temperature
ρ_0 = density of the melt
Φ_0 = electric potential scale
σ = electrical conductivity
ϕ = shape function for velocity
θ = shape function for temperature
ψ = shape function for pressure
$\mathbf{\Phi}$ = disctertized electric potential vector
$\partial\Omega$ = boundary of computational domain
∇ = gradient operator

Subscripts

i,j = the ith, jth point
n = the nth component
μ = viscosity related

Superscripts

i,j = the ith, jth component
T = matrix transpose

1. Introduction

Space experiments have revealed that solute striations in space-grown crystals are primarily caused by the melt convection generated by residual gravity forces, or g-jitter, associated with space vehicles such as the Space Shuttles and the International Space Station. Signatures registered by on-board accelerometers indicate that g-jitter perturbations are random in both direction and time and are attributed to a variety of sources including atmospheric drag, solar radiation, thruster firings, pump and other mechanical component operations, and astronaut exercises (Alexander and Banish, 1998). One set of g-jitter data recorded during a space flight is shown in Figure 1. While small, these perturbed gravity forces can produce complex, irregular, three-dimensional (3D) convective flows in the melt

pool, which are blamed for non-uniform solute distributions and other defects formed in the crystals grown in space (de Groh and Nelson, 1994).

There has been substantial work on convective flows in single crystal growth systems induced by *g*-jitter perturbations in space. Both steady state and transient *g*-jitter effects have been considered. Findings from these studies may be summarized as follows. The frequency, amplitude and spatial orientation of the *g*-jitter all play an important role in affecting the convective flows. The most detrimental effects of *g*-jitter come from the low frequency components with large amplitudes, especially when they are acting perpendicularly to the temperature gradient imposed for the growth of crystals from their melts (Alexander *et al.*, 1989, 1991; Kamotani *et al.*, 1995; Tang *et al.*, 1996; Monti and Savino, 1998; Li *et al.*, 2003). For semiconductor single crystal growth applications, the effects of the high frequency *g*-jitter components may be neglected (Alexander *et al.*, 1989, 1991).

Magnetic damping of the motion of an electrically conducting fluid stems from the interaction between the convection and an applied magnetic field, which generates an

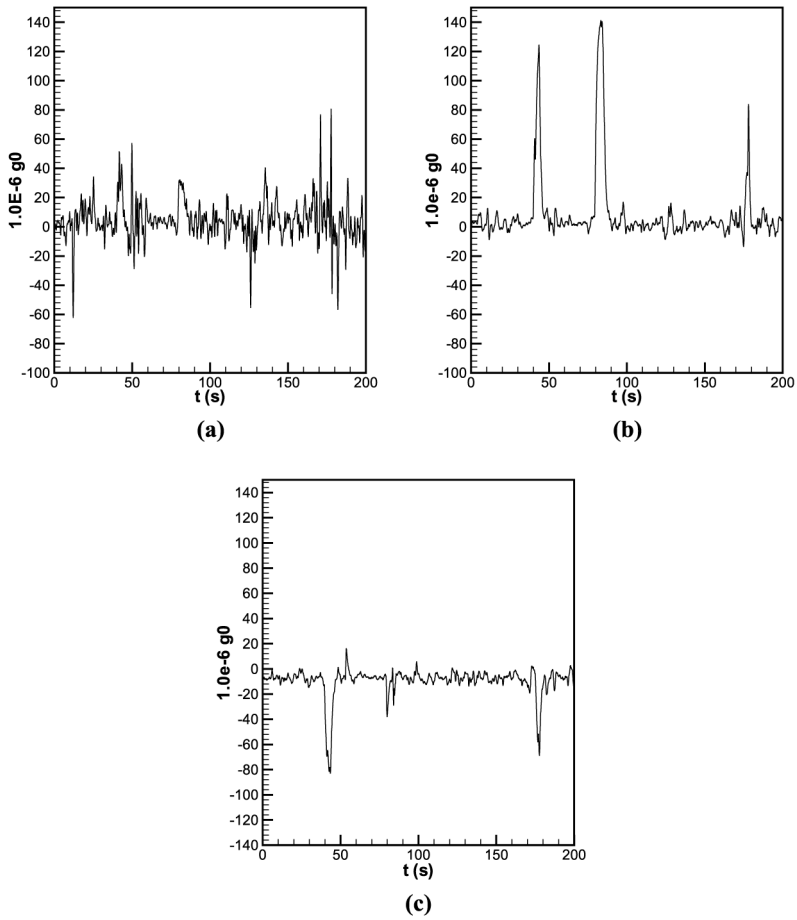

Figure 1.
Signature of *g*-jitter data in the *x*-, *y*- and *z*-directions as function of time registered by an accelerometer aboard the Space Shuttle, where time is measured in seconds

opposing Lorentz force to suppress the flows. While magnetic damping has been widely exploited to obtain more homogeneous semiconductors and metal crystals under terrestrial conditions (Series and Hurle, 1991), relatively little has been done on the magnetic damping of the deleterious effects associated with low frequency *g*-jitter during space crystal growth. Recently, analytical, asymptotic and numerical analyses have been performed for two-dimensional (2D) geometries related to space processing (Li, 1996, 2001; Pan and Li, 1998; Shang *et al.*, 2001; Ma and Walker, 1996). These analyses show that magnetic fields can provide an effective means to damp the *g*-jitter induced convective flows. While these 2D models have been very useful in developing a fundamental understanding, they are inadequate to address other many issues crucial to space experiments design and system performance. For example, *g*-jitter is known to be 3D and time-dependent in nature and is conceived to drive a spatially and temporally irregular 3D flow, which obviously cannot be faithfully described by a 2D model. Also, how the 3D flow structure develops in space and time and how the flow affects the thermal and solute transport in the melt in a space environment are not well understood. Moreover, the behavior of the time-evolving 3D flow and its interaction with an applied magnetic field are even less appreciated. Despite their popularity, the limitations and validity of the 2D models for *g*-jitter induced flows with and without an applied field have not yet been established. Undoubtedly, full 3D models are required to adequately address these issues.

This paper presents a full 3D transient finite element model for magnetic damping on *g*-jitter induced fluid flow and heat and mass transfer in an idealized Bridgman system for the melt growth of the Ga-doped germanium single crystal in space. The model development is based on the Galerkin finite element solution of magnetohydrodynamic equations governing the fluid flow and heat and mass transfer in the presence of time dependent gravity perturbations and applied magnetic fields. Both synthetic *g*-jitter and real *g*-jitter data are used in the analyses.

2. Problem statement

Figure 2 shows the simplified 3D model for the Bridgman system for Ga-doped germenium single crystal growth in microgravity, along with the coordinate system used for the numerical analyses. The simplification comes from neglecting the solidification phenomena by assuming a flat solid-liquid interface as a first approximation. A 2D model of this type, whose limitations and validity will be checked against the 3D model, has been studied extensively in literature and the justification of the simplification is documented (Alexander *et al.*, 1989, 1991), who suggested that for melt flow study, a flat solid-liquid interface serves a good approximation. Referring to Figure 2, the melt is fed from inlet into the melt pool while the single crystal is withdrawn from below. Both the dependence of melting temperature on solute concentration and the solutal expansion coefficient are neglected, because the solute concentration being considered is dilute and the solutal expansion coefficient is small (Alexander *et al.*, 1989, 1991). For the present configuration, the lower side marked by h_2 is insulated and the upper wall is fixed at the same temperature as the top surface or the melt inlet. This specific configuration is chosen, also because it can be used to compare with the results obtained from its 2D counterparts (Alexander *et al.*, 1989, 1991; Shang *et al.*, 2001).

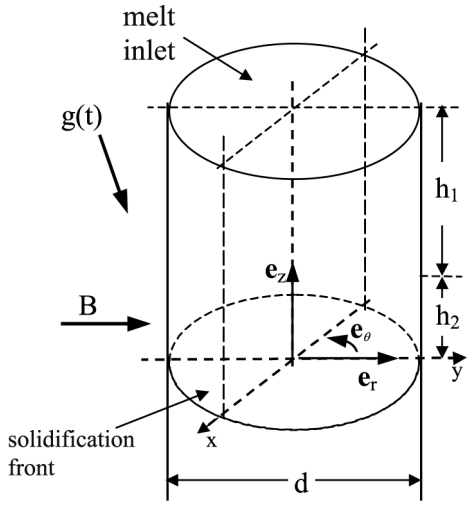

Figure 2.
Schematic representation of the simplified model of 3D Bridgman crystal growth system

The physical phenomena occurring in the system described above are governed by the Maxwell equations for the electromagnetic field distribution, the Navier-Stokes equations for fluid flow and the scalar transport equations for both heat and mass transfer. For laboratory systems such as the one being considered, the magnetic Reynolds number is small. Consequently, the induced magnetic field is negligible in comparison with the imposed magnetic field and so does the time variation of the induced electric field (Li, 1996; Pan and Li, 1998). These considerations allow us to reduce the Maxwell equations to one scalar equation for the electric potential (Li, 1996). With these simplifications and further with the Boussinesq approximation, the non-dimensional governing equations for the 3D transient model may be written as follows:

$$\nabla \cdot \mathbf{u} = 0 \tag{1}$$

$$\frac{\partial \mathbf{u}}{\partial t} + \mathbf{u} \cdot \nabla \mathbf{u} = -\nabla p + Pr\,\nabla^2 \mathbf{u} - Ra\,Pr\,T\mathbf{g}^* + Ha^2\,Pr(-\nabla\Phi + \mathbf{u} \times \mathbf{B}) \times \mathbf{B} \tag{2}$$

$$\frac{\partial T}{\partial t} + \mathbf{u} \cdot \nabla T = \nabla^2 T \tag{3}$$

$$\frac{Sc}{Pr}\left(\frac{\partial C}{\partial t} + \mathbf{u} \cdot \nabla C\right) = \nabla^2 C \tag{4}$$

$$\nabla^2 \Phi = \nabla(\mathbf{B} \times \mathbf{u}) = \mathbf{B}(\nabla \times \mathbf{u}) \tag{5}$$

In deriving the above dimensionless equations, the following scales have been used: $L_0 = d$, $U_0 = \kappa/L_0$, $t_0 = L_0^2/\kappa$, $P_0 = \rho_0 U_0^2$ and $\Phi_0 = \kappa B_0$. Referring to Figure 2, the boundary conditions are phrased in mathematical terms:

$$T = 0 \quad \text{at } z = 0 \tag{6}$$

$$\mathbf{u}\cdot\mathbf{n} = \frac{Pe_g Pr}{Sc} \quad \text{at } z = 0 \tag{7}$$

$$\mathbf{u}\times\mathbf{n} = 0 \quad \text{at } z = 0 \tag{8}$$

$$\mathbf{n}\cdot\nabla C = Pe_g(1-k)C \quad \text{at } z = 0 \tag{9}$$

$$T = 1 \quad \text{at } z = 1 \tag{10}$$

$$\mathbf{u}\cdot\mathbf{n} = -\frac{Pe_g Pr}{Sc} \quad \text{at } z = 1 \tag{11}$$

$$\mathbf{u}\times\mathbf{n} = 0 \quad \text{at } z = 1 \tag{12}$$

$$\mathbf{n}\cdot\nabla C = -Pe_g(C-1) \quad \text{at } z = 1 \tag{13}$$

$$\mathbf{u}\cdot\mathbf{n} = \frac{Pe_g Pr}{Sc} \quad \text{at } r = 0.5 \tag{14}$$

$$\mathbf{u}\times\mathbf{n} = 0 \quad \text{at } r = 0.5 \tag{15}$$

$$\mathbf{n}\cdot\nabla C = 0 \quad \text{at } r = 0.5 \tag{16}$$

$$T = 1 \quad \text{at } r = 0.5,\ h_1/d < z < 1 \tag{17}$$

$$\mathbf{n}\cdot\nabla T = 0 \quad \text{at } r = 0.5,\ 0 < z < h_1/d \tag{18}$$

$$\mathbf{n}\cdot\nabla\Phi = 0 \quad \text{at } z = 0, 1,\ r = 0.5 \tag{19}$$

Note that equation (19) basically states that the normal component of the electric current density is zero on the solid walls, because the walls are electrically insulated. The boundary conditions are the extension of 2D model presented elsewhere (Shang *et al.*, 2001).

3. Numerical method

The above equations along with the boundary conditions are solved using the Galerkin finite element method. Following the procedures in previous studies (Shang *et al.*, 2001; Song and Li, 2001), the governing equations are recast in integral forms

$$\mathbf{M}_U\dot{\mathbf{U}} + \mathbf{K}_U(\mathbf{U})\mathbf{U} + \frac{1}{\varepsilon}\mathbf{C}_P\mathbf{M}_P\mathbf{C}_P^{\mathrm{T}}\mathbf{U} + \mathbf{B}_B\mathbf{T} + \mathbf{B}_U\mathbf{U} = \mathbf{F}_{\mathrm{U}} \tag{20}$$

$$\mathbf{M}_T\dot{\mathbf{T}} + \mathbf{K}_T(\mathbf{U})\mathbf{T} = \mathbf{F}_T \tag{21}$$

$$\mathbf{M}_C\dot{\mathbf{C}} + \mathbf{K}_C(\mathbf{U})\mathbf{C} = \mathbf{F}_C \tag{22}$$

$$\mathbf{K}_\Phi\mathbf{\Phi} + \mathbf{B}_\Phi\mathbf{U} = \mathbf{F}_\Phi \tag{23}$$

where the matrices are calculated by the following expressions:

$$\mathbf{M}_P = \int_\Omega \psi\psi^{\mathrm{T}}\,\mathrm{d}V; \quad \mathbf{M}_{\mathrm{T}} = \int_\Omega \theta\theta^{\mathrm{T}}\,\mathrm{d}V$$

$$\mathbf{M}_U = \int_\Omega \phi\phi^{\mathrm{T}}\,\mathrm{d}V; \quad \mathbf{M}_C = \int_\Omega \frac{Sc}{\mathrm{Pr}}\theta\theta^{\mathrm{T}}\,\mathrm{d}V$$

$$\mathbf{D}_U = \int_\Omega Pr\nabla\theta\cdot\nabla\theta^{\mathrm{T}}\,\mathrm{d}V; \quad \mathbf{D}_C = \int_\Omega \nabla\theta\cdot\nabla\theta^{\mathrm{T}}\,\mathrm{d}V$$

$$\mathbf{D}_T = \int_\Omega \nabla\theta\cdot\nabla\theta^{\mathrm{T}}\,\mathrm{d}V; \quad \mathbf{K}_\Phi = \int_\Omega \nabla\theta\cdot\nabla\theta^{\mathrm{T}}\,\mathrm{d}V$$

$$\mathbf{A}_U(\mathbf{U}) = \int_\Omega \phi\,\mathbf{u}\cdot\nabla\theta^{\mathrm{T}}\,\mathrm{d}V; \quad \mathbf{A}_T(\mathbf{U}) = \int_\Omega \theta\,\mathbf{u}\cdot\nabla\theta^{\mathrm{T}}\,\mathrm{d}V$$

$$\mathbf{A}_C(\mathbf{U}) = \int_\Omega \frac{Sc}{Pr}\theta\,\mathbf{u}\cdot\nabla\theta^{\mathrm{T}}\,\mathrm{d}V; \quad \mathbf{B}_T = \int_\Omega (RaPr\mathbf{g}\phi\theta^{\mathrm{T}})\mathrm{d}V$$

$$\mathbf{B}_U = \int_\Omega \phi^{\mathrm{T}}\,\mathbf{B}\cdot\nabla\theta^{\mathrm{T}}\,\mathrm{d}V; \quad \mathbf{B}_\Phi = \int_\Omega \theta\mathbf{B}\cdot\nabla\times(\theta^{\mathrm{T}}\hat{\mathbf{u}})\mathrm{d}V$$

$$\mathbf{H}_U = -\int_\Omega \phi Ha^2Pr(\phi^{\mathrm{T}}\hat{\mathbf{u}}\times\mathbf{B}\times\mathbf{B})\mathrm{d}V; \quad \mathbf{F}_U = \int_{\partial\Omega}\mathbf{n}\cdot\tau\phi\,\mathrm{d}S$$

$$\mathbf{F}_C = -\int_{\partial\Omega} q_C\theta\,\mathrm{d}S; \quad \mathbf{F}_T = -\int_{\partial\Omega} q_T\theta\,\mathrm{d}S$$

$$\mathbf{K}_U(\mathbf{U}) = \mathbf{D}_U + \mathbf{A}_U(\mathbf{U}) + \mathbf{H}_U; \quad \mathbf{K}_T(\mathbf{U}) = \mathbf{D}_T + \mathbf{A}_T(\mathbf{U})$$

$$\mathbf{K}_C(\mathbf{U}) = \mathbf{D}_C + \mathbf{A}_C(\mathbf{U}); \quad \mathbf{C}_P = \int_\Omega \nabla\phi\psi^{\mathrm{T}}\,\mathrm{d}V$$

The above matrix equations are solved using the successive substitution method and the time derivatives are approximated using the implicit finite difference scheme.

4. Some computational aspects

Equations (20)-(23), formulated as above, represent an extremely computationally intensive task when the LU decomposition method is used to invert the matrix, even with all necessary speed-improving measures such as skyline storage and an optimized heuristic re-numbering scheme. To see this, the final finite element global matrix assembled from equations (20)-(23) is given in equation (24) below

$$\begin{bmatrix} \mathbf{M} & \mathbf{0} & \mathbf{0} & \mathbf{0} \\ \mathbf{0} & \mathbf{M}_T & \mathbf{0} & \mathbf{0} \\ \mathbf{0} & \mathbf{0} & \mathbf{M}_C & \mathbf{0} \\ \mathbf{0} & \mathbf{0} & \mathbf{0} & \mathbf{0} \end{bmatrix} \begin{bmatrix} \dot{\mathbf{U}} \\ \dot{\mathbf{T}} \\ \dot{\mathbf{C}} \\ \dot{\mathbf{\Phi}} \end{bmatrix} + \begin{bmatrix} \mathbf{K}_U + \frac{1}{\varepsilon}\mathbf{C}_P\mathbf{M}_P^{-1}\mathbf{C}_P^{\mathrm{T}} & \mathbf{B}_T & \mathbf{B}_C & \mathbf{B}_\Phi \\ \mathbf{0} & \mathbf{K}_T & \mathbf{0} & \mathbf{0} \\ \mathbf{0} & \mathbf{0} & \mathbf{K}_C & \mathbf{0} \\ \mathbf{B}_U & \mathbf{0} & \mathbf{0} & \mathbf{K}_\Phi \end{bmatrix} \begin{bmatrix} \mathbf{U} \\ \mathbf{T} \\ \mathbf{C} \\ \mathbf{\Phi} \end{bmatrix} = \begin{bmatrix} \mathbf{F}_U \\ \mathbf{F}_T \\ \mathbf{F}_C \\ \mathbf{F}_\Phi \end{bmatrix} \tag{24}$$

Tests on a SGI supercomputer (Onyx model) machine showed that each non-linear iteration required about 120 CPU minutes for a 3D model consisting of 5,304 nodes (see Figure 3 and Section 4.1 below). A typical transient simulation requires about 1,000 time steps and within each step about 3-4 iterations are needed to converge. This means that a complete run would require about one year CPU time, which clearly is an impractical task.

On the other hand, matrix given by equation (24) has a very significant number of unfills during the LU decomposition, which is a bottleneck for computational speed, and the use of various heuristic re-numbering algorithms did not seem to alleviate the problem much. Examination of the matrix structure, however, suggests that all the **B** submatrices may be moved to the right side through simple matrix operations so as to substantially reduce the bandwidth of the final matrix and hence the number of unfills. For a flow simulation where flow velocity is not high, such as the case being considered, matrices $\mathbf{B}_T$ and $\mathbf{B}_C$ may be put on the right-hand side with a decreased numerical performance. This physics-based re-arranging, which is based on weather or not the interaction between the fields is strong, is followed by re-numbering the final matrix by re-grouping $\mathbf{K}_T$, $\mathbf{K}_C$ and $\mathbf{K}_\Phi$ into three separate matrices, each stored in a skyline format. This procedure has greatly reduced computational burdens associated

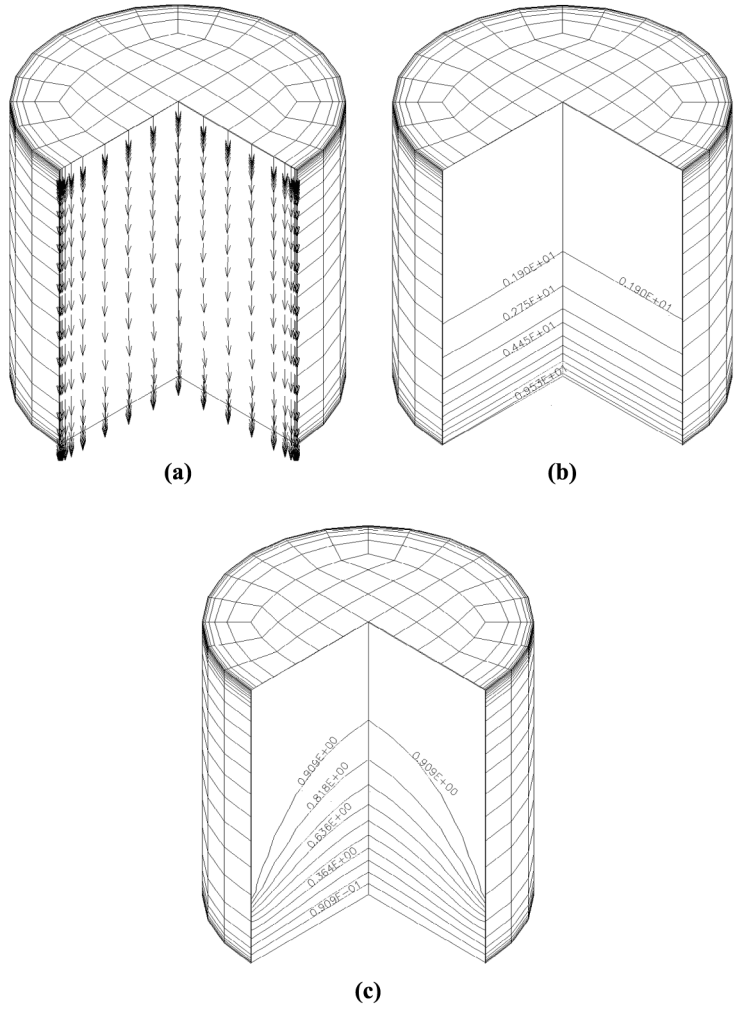

Figure 3.
The 3D view of (a) flow field; (b) solute concentration distribution; and (c) temperature distribution with the steady state microgravity in the *x*-direction

with the 3D simulations. Indeed, numerical tests show that a factor of about 120 in speed increase is achieved with this arrangement, compared with the traditional skyline-LU based approach. A crucial step contributed to this drastic increase in the computational speed involves re-designing the global matrix skyline structure to pre-eliminate the unfills and a suitable LU solver that takes advantage of this re-designed matrix structure. Also, this formulation requires an iterative procedure and a tighter convergence criterion. For example, for the results to have the same accuracy as the case when the force is included in the global matrix, the convergence criterion for non-linearity at each time step has to set at the relative tolerance of 1×10^{-5} instead of 1×10^{-4}. Fortunately, the convergence is very fast and at the worst scenario case additional 2 or 3 iterations were required in comparison with the

standard formulation. While not pursued in this study, a further increase in computational speed may be possible by applying a parallel algorithm such that matrices for the scalar quantities are calculated using a separate processor. The re-arrangement described here should make it easy to design such a parallel computational scheme.

5. Results and discussion

The finite element model described above enables the prediction of both steady and transient thermal convection and heat and mass transfer in single crystal growth systems under both terrestrial and microgravity conditions with and without presence of applied magnetic fields. The model development is based on the modification of the finite element code reported in early studies (Shang *et al.*, 2001; Song and Li, 2001), which include both code development and benchmark testing for thermal and fluid flow calculations. The thermo-physical properties and geometric dimensions for the study are given in Table I. The field variables have converged within a pre-set relative tolerance of 1×10^{-5}. Numerical simulations were carried out for a wide range of conditions and a selection of the computed results is presented below.

5.1 Mesh independence test

Before calculations were carried out, mesh dependency was tested for numerical simulations. A variety of mesh size and distributions was tested and the final finite element mesh used for the results presented below is shown in Figure 3, which

	Value
Property	
K	$17\,\mathrm{W\,K^{-1}\,m^{-1}}$
C_p	$0.39\,\mathrm{J\,g^{-1}\,K^{-1}}$
ρ	$5.6 \times 10^{3}\,\mathrm{Kg\,m^{-3}}$
ν	$1.3 \times 10^{-7}\,\mathrm{m^2\,s^{-1}}$
D	$1.3 \times 10^{-8}\,\mathrm{m^2\,s^{-1}}$
κ	$1.3 \times 10^{-5}\,\mathrm{m^2\,s^{-1}}$
β	$2.5 \times 10^{-4}\,\mathrm{K^{-1}}$
Dimensionless parameters	
Pr	0.01
Pe	5.0
Ra	1.45×10^{5} (based on g_0)
Ha	100
Sc	10
Scale parameters	
U_0	1.3×10^{-3}
t_0	100/13
Operating conditions	
T_h	1331 K
L	0.01 m
T_m	1231 K
V_m	$6.5 \times 10^{-6}\,\mathrm{m\,s^{-1}}$
g/f	$g_0 \times 10^{-3}$/0.1 Hz
B_0	0.022-0.22 T

Table I.
Parameters used in calculations

employed 5,304 8-node brick elements with an increasing mesh distribution near the boundary. In determining the final mesh, a criterion used for mesh-independence check is that two consecutive reductions in mesh size (reduced by half) produce a relative error of the maximum velocities less than 0.1 percent. The test was done using the steady state data with $g = g_0 \times 10^{-3}$ with $Ha = 100$ and further checked with $Ha = 0$. It is noted here that for magnetic damping problems under consideration, a Hartmann layer may persist near the walls. For high velocity flows, this layer may cause difficulty in numerical simulations. Numerical experiments with various cases showed that for the conditions and configurations under consideration, a placement of 3-5 finite elements in the layer is able to provide needed accuracy.

5.2 Steady state calculations

The gravity level of an achievable dynamic weightlessness condition is $g_0 \times 10^{-6}$. Numerical simulations were carried out for this condition, and the results are helpful in gaining physical insights into the steady state behavior of the system. They are also the required initial condition for the dynamic behavior of the system when *g*-jitter sets in. The simulations were based on the direct numerical solution to the steady state governing equations obtained by dropping out the time dependent terms in the model equations described in Section 2, while retaining all the mutually coupled terms. In present study, the gravity orientation is assumed to be perpendicular to the temperature gradient, say in the *x*-direction, which represents the worst scenario case. The computed flow field, solute concentration distribution and temperature distribution are shown in Figure 3. Apparently, the gravity has negligible effects on the flow field, and the crystal pulling velocity controls the flow field (Figure 3(a)). The solute concentration distribution is nearly parallel to solidification front (Figure 3(b)), representing a nearly idealized purely diffusion controlled growth condition. The temperature distribution is mainly controlled by the thermal conduction (Figure 3(c)), and the thermal field remains basically the same even when the *g*-jitter induced convection occurs. This is a direct result of small *Pr* number for the system being studied. Thus the temperature distribution study is ignored thereafter. Moreover, all the field variable distributions are nearly axisymmetric. The above results are qualitatively consistent with those obtained from a 2D simplified crystal growth system (Shang *et al.*, 2001).

The 3D model also has been applied to study convective flows under other microgravity conditions. One of the important issues that a 2D model has not yet been able to answer is the 3D nature of the convective flows. Figure 4 shows the parallel projection of plane-cut views of flow patterns obtained from the 3D models for different levels of low gravity forces acting in the *x*-direction. Two types of plane-cuts are made: one is the *x-z* (or $y = 0$) plane (Figure 4(a) and (c)) and the other the *y-z* (or $x = 0$) plane (Figure 4(b) and (d)). In comparison with the published 2D model results (Alexander *et al.*, 1991; Shang *et al.*, 2001), the flow fields depicted in the *x-z* plane (Figure 4(a), (c)) almost reproduce the 2D results, suggesting that a two-model indeed provides a reasonably good representation of low gravity induced flows there. On the other hand, the flow fields in the *y-z* plane (Figure 4(d)) reveal that a complex 3D convective flow structure is developed when gravity increases to the level of $g_0 \times 10^{-3}$, which is obviously beyond any 2D description.

An applied magnetic field is known to provide a damping mechanism for convective flows. The flow patterns in the *x-z* and *y-z* planes obtained from the 3D model with an applied magnetic field oriented in the *z*-direction are shown in Figure 4(e) and (f). Comparison of the results in Figure 4 shows that an applied magnetic field is effective in suppressing the low-gravity driven convective flows. The maximum velocities of the flow field as a function of gravity level and applied magnetic field strength are presented in Table II. Apparently, the maximum velocity decreases almost linearly as the magnitude of the gravity decreases. This relation also holds true in the presence of the magnetic field. For the cases with the same gravity level, a higher magnetic field produces a stronger damping effect.

5.3 Single frequency g-jitter

The Fourier analysis of gravity measurements from accelerometers aboard the Space Shuttles shows that *g*-jitter covers a wide range of frequency spectrum. A single Fourier component of the synthesized *g*-jitter is useful in providing insightful information on the general behavior of the fluid flow under the influence of the *g*-jitter. Here, we consider a case in which *g*-jitter takes the form of $g(t) = g_0 \times 10^{-3}\sin(0.2\pi t)$ acting in the *x*-direction and sets in to perturb the steady state condition discussed above. The time evolution of maximum velocity in the melt, as the *g*-jitter disturbances take effect, is shown in Figure 5. Here, it is seen that the melt convection evolves eventually into a *quasi-steady* time-harmonic oscillating motion. Note that in calculating the maximum velocities, the absolute values have been used. As one might have expected, the flow field is complex, 3D and time evolving, which is illustrated by the snapshot plots of the convection fields in Figures 6 and 7 over a time period after the flow reaches the *quasi-steady* state. In the *x-z* plane (Figure 6), the convection loop oscillates and reverses its rotating direction at approximately the same frequency of the driving *g*-jitter force. The convection sweeps back and forth along the growth front and causes the solute concentration distribution non-uniformity at the lower solid-liquid interface. The similar flow field patterns were obtained with 2D models (Alexander *et al.*, 1991; Shang *et al.*, 2001), suggesting again that a 2D model is capable of predicting the velocity profiles reasonably well in the *x-z* plane when *g*-jitter acts in the *x*-direction. The flow field pattern in the *y-z* plane is more complex (Figure 7), clearly displaying the 3D nature of the *g*-jitter driven convection. The time evolution of the flow, however, appears to follow the same oscillation frequency as the driving

g-jitter	U_{max}
$g = g_0 \times 10^{-3}$	0.463
$g = g_0 \times 10^{-4}$	5.56×10^{-2}
$g = g_0 \times 10^{-5}$	9.83×10^{-3}
$g = g_0 \times 10^{-6}$	5.48×10^{-3}
$g = g_0 \times 10^{-3}$ with **B**	2.06×10^{-2}
$g = g_0 \times 10^{-4}$ with **B**	6.56×10^{-3}
$g = g_0 \times 10^{-5}$ with **B**	5.16×10^{-3}
$g = g_0 \times 10^{-6}$ with **B**	5.02×10^{-3}

Table II.
The dependence of U_{max} on gravity level

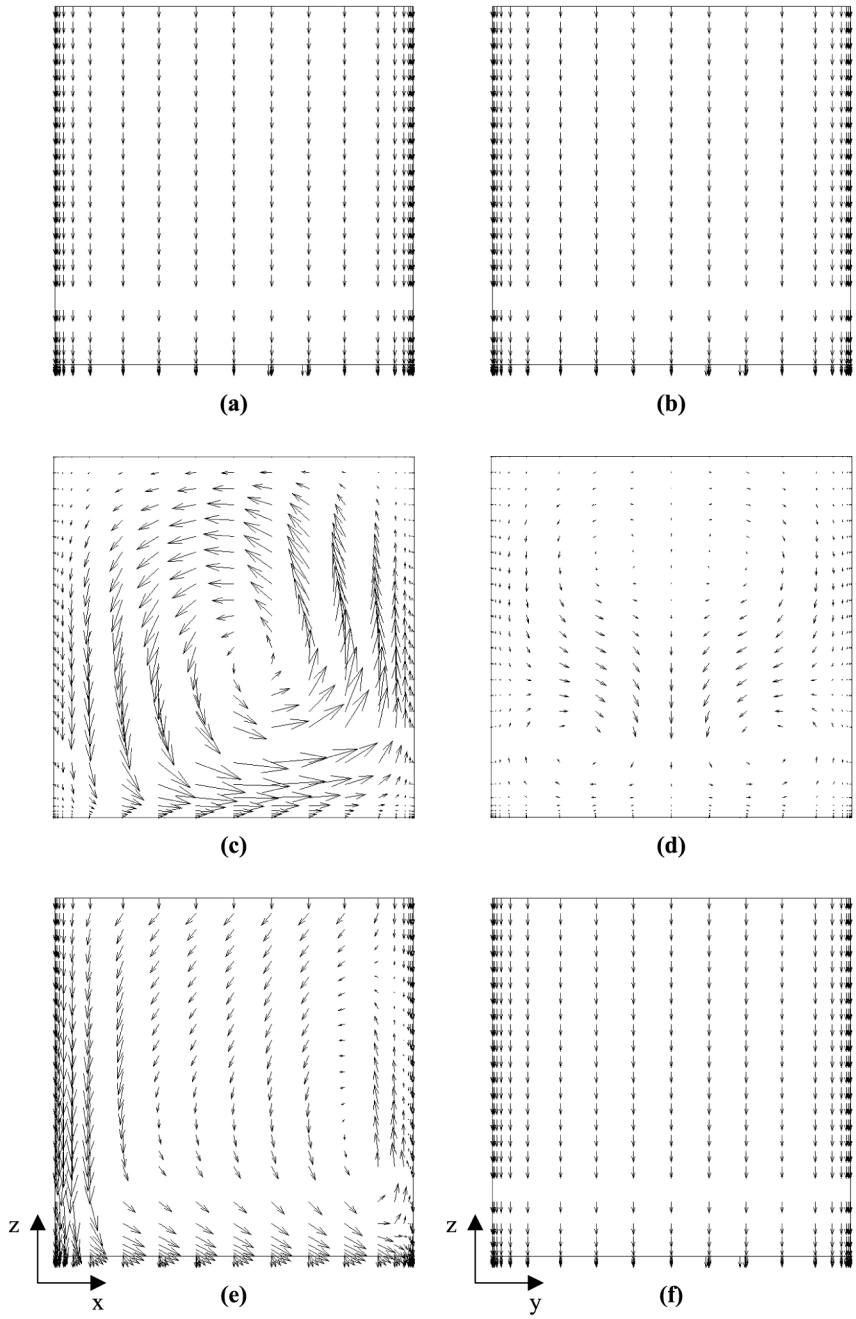

Figure 4.
Plane-cut views of the flow field induced by low gravity in x-direction without magnetic field (a) x-z plane with $g = 10^{-6}$; (b) y-z plane with $g = 10^{-6}$; (c) x-z plane with $g = 10^{-3}$; (d) y-z plane with $g = 10^{-3}$, and with magnetic field $B = 0.22$ T ($Ha = 100$) in z-direction; (e) x-z plane with $g = 10^{-3}$; (f) y-z plane with $g = 10^{-3}$

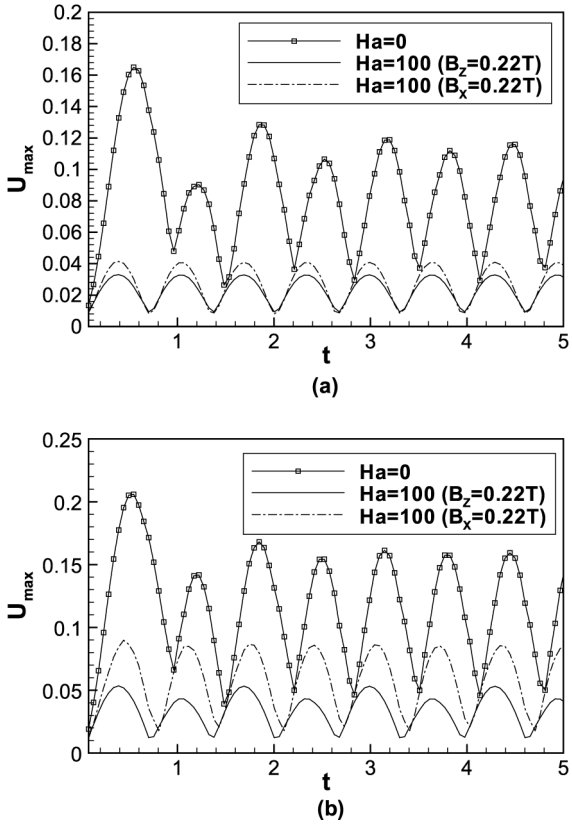

Figure 5.
History of transient maximum flow velocity induced by the single frequency *g*-jitter ($10^{-3}\sin(0.2\pi t)$) acting in (a) *x*-direction; and (b) *x-y-z* direction without magnetic field and with magnetic field $B = 0.22$ T ($Ha = 100$) in the *x*- or *z*-direction, respectively

g-jitter. Computed results were also obtained with *g*-jitter oriented in other directions such as the *x-y* or *x-y-z* direction. The findings are qualitatively the same as above in that a 2D model is useful in providing a good approximation of the flow field in the symmetry plane parallel to the *g*-jitter direction, for instance, in the *x-y-z* symmetry plane when the gravity is oriented in the *x-y* direction, while in other planes, full 3D models are required to unlock the mystery of the complex 3D flow structures. The time evolution of maximum velocity in the melt, as the *g*-jitter disturbances take effect in *x-y-z* direction, is also shown in Figure 5.

Numerical simulations were also conducted with a magnetic field applied in the *x*- or *z*-direction to understand the damping effects of the field on the complex 3D transient *g*-jitter induced flows as discussed above. The computed results for the maximum velocity in the melt are also shown in Figure 5. Inspection of these results illustrates that an applied magnetic field is also effective in suppressing the transient *g*-jitter induced flows and, more importantly, the field in *z*-direction has the most significant damping effect for the system studied here. This holds true irrespective of *g*-jitter orientations. Additional 3D numerical simulations agree with the findings obtained from the previous 2D damping model (Shang *et al.*, 2001) that the magnetic damping effect becomes stronger with an increase of the applied field strength. Analysis of the

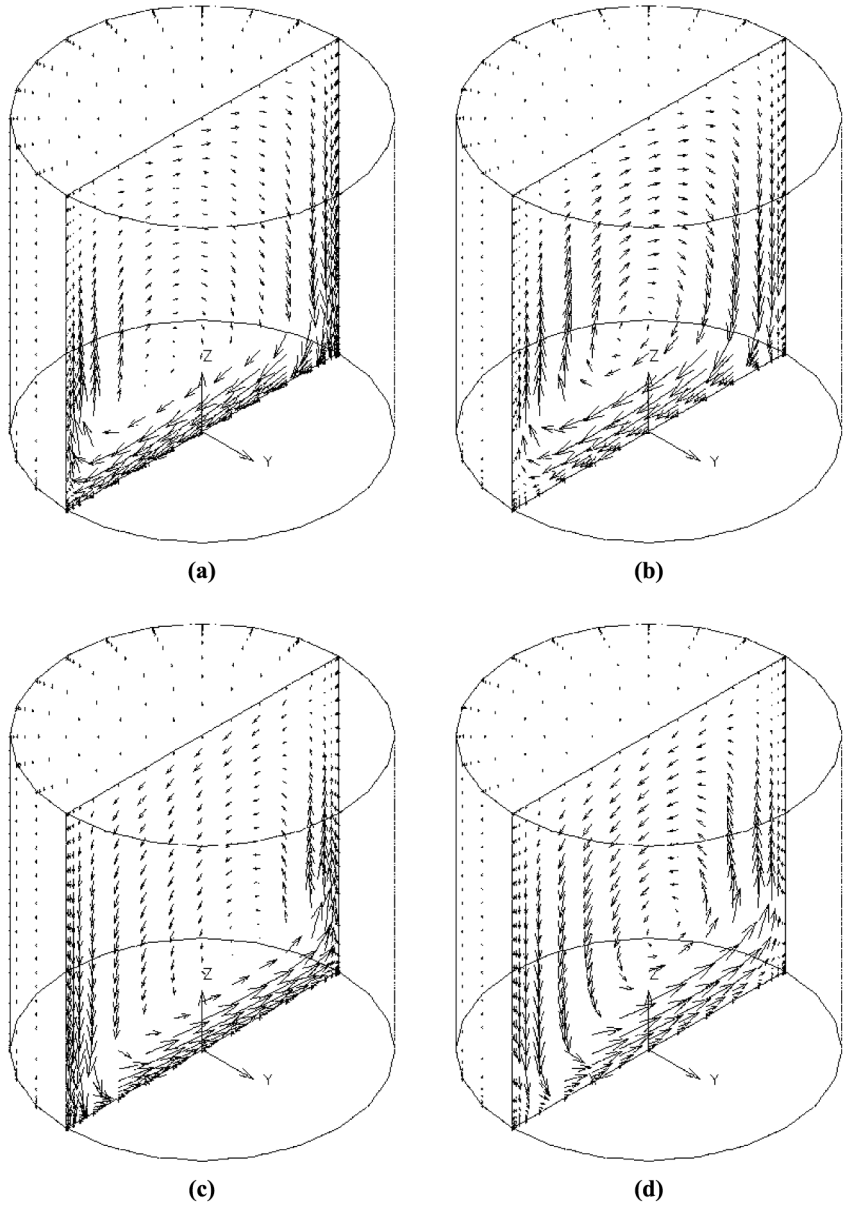

Figure 6.
The flow field patterns in x-z plane with the single frequency g-jitter perturbation acting in x-direction without applied magnetic field in one time-harmonic period of the driving force (a) $t = 5.525, U_{max} = 0.0702$; (b) $t = 5.85, U_{max} = 0.0953$; (c) $t = 6.175, U_{max} = 0.0702$; (d) $t = 6.5, U_{max} = 0.0953$

3D flow structures and their time evolution patterns shows that the 3D flow patterns are similar to those without the magnetic field, but with much weaker flow intensity. For example, compared with the case without the magnetic field, the maximum velocities of the flow field (U_{max}) at time $t = 5.525$ and $t = 6.175$ are reduced by more than 50 percent when the field is applied (Figure 8). These convective flows oscillate

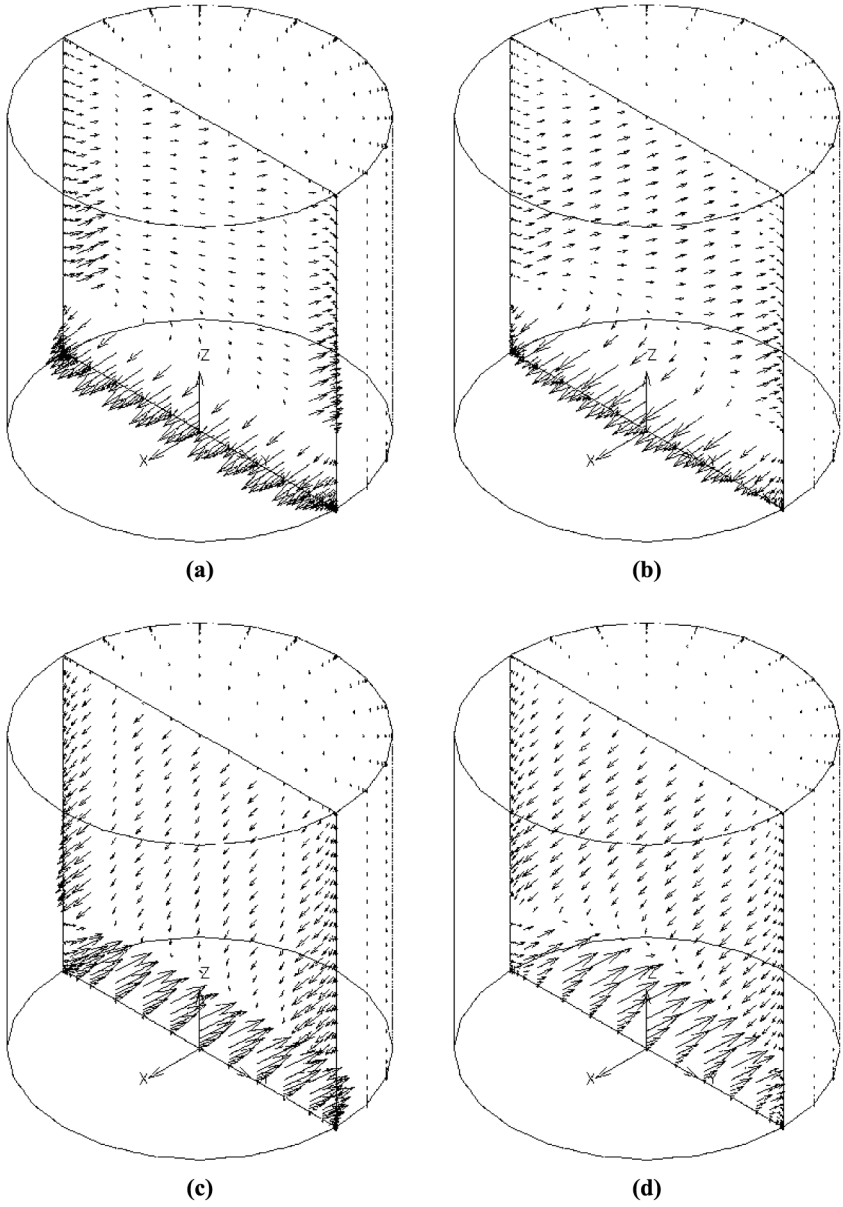

Figure 7.
The flow field patterns in the y-z plane with the single frequency g-jitter perturbation acting in x-direction without applied magnetic field in one time-harmonic period of the driving force (a) $t = 5.525$, $U_{max} = 0.0702$; (b) $t = 5.85$, $U_{max} = 0.0953$; (c) $t = 6.175$, $U_{max} = 0.0702$; (d) $t = 6.5$, $U_{max} = 0.0953$

time-harmonically at the same frequency of g-jitter, but with a phase lag that is also a function of the applied magnetic field. These observations are also consistent with the 3D simulations obtained for other orientations and magnitudes of the g-jitter and magnetic fields.

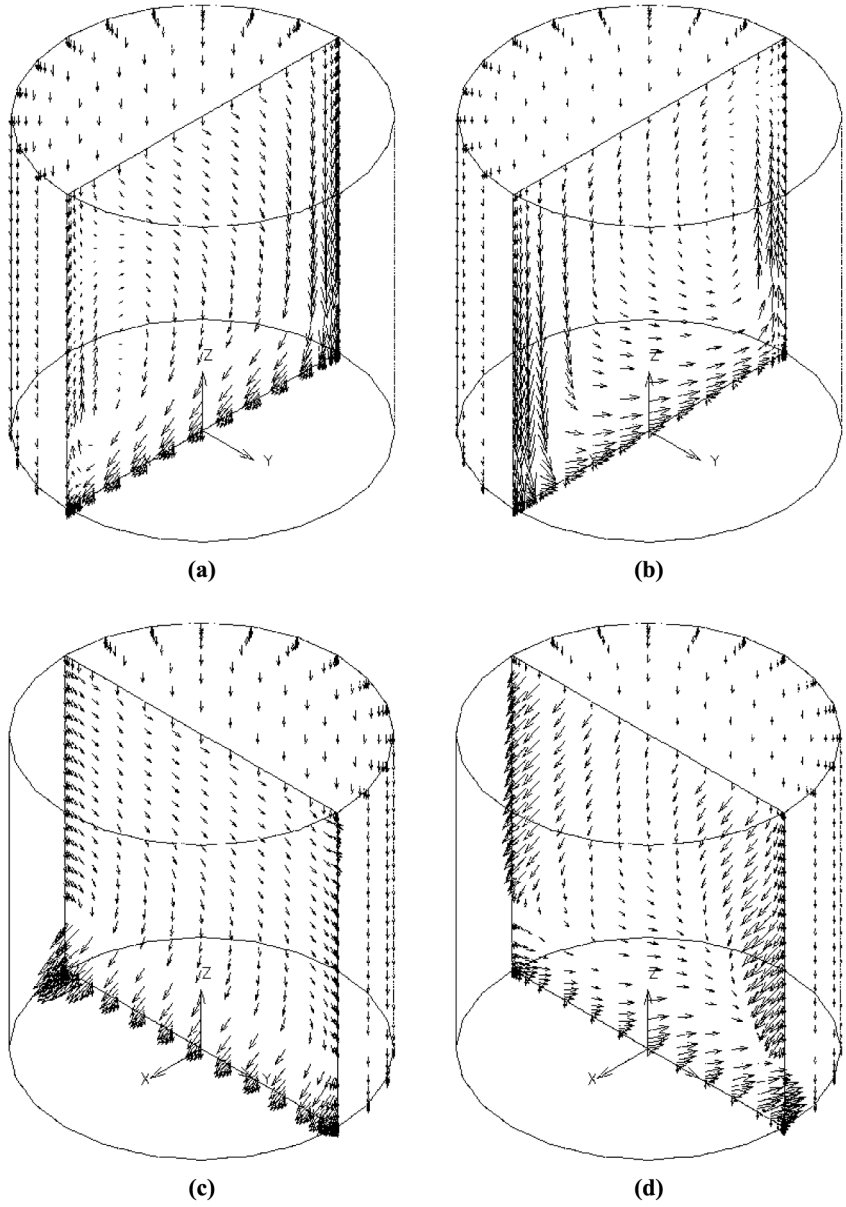

Figure 8.
The flow field patterns with the single frequency *g*-jitter perturbation acting in *x*-direction in presence of applied magnetic field in *z*-direction in (a) *x-z* plane, $t = 5.525, U_{max} = 0.0248$; (b) *y-z* plane, $t = 5.525, U_{max} = 0.0248$; (c) *x-z* plane, $t = 6.175, U_{max} = 0.0318$; (d) *y-z* plane, $t = 6.175, U_{max} = 0.0318$

The effects of *g*-jitter on the solute transport in the melt with and without an applied magnetic field, which are the major concern of a space flight, are shown in Figure 9. The solute concentration distribution significantly deviates from the diffusion-controlled growth mechanism and reveals the strong effect of *g*-jitter induced convection on the solute transport (Figure 9(a) and (b)). The convection results

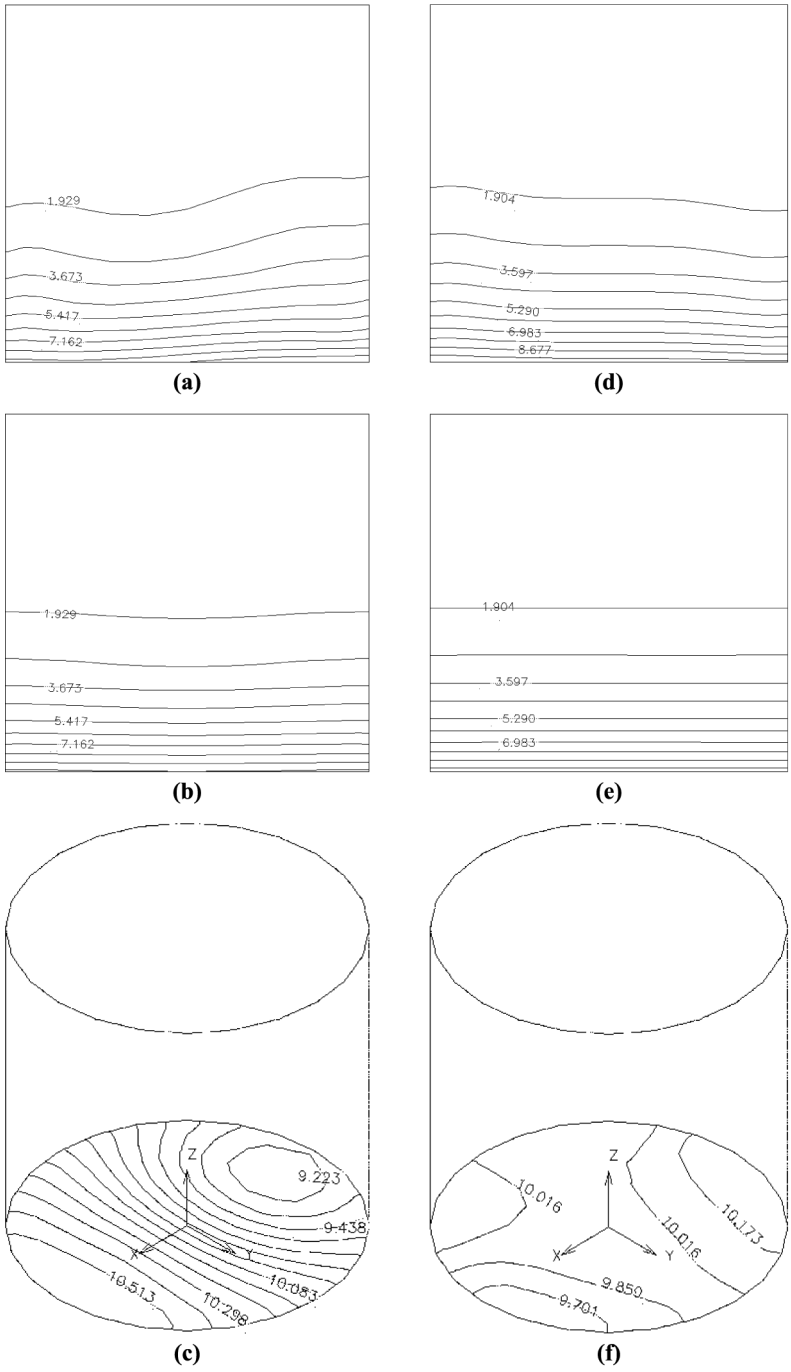

Figure 9.
Plane-cut views of the solute concentration distribution induced by single frequency *g*-jitter ($10^{-3}\sin(0.2\pi t)$) acting in *x*-direction without magnetic field (a) *x-z* plane; (b) *y-z* plane; (c) growth interface, and with magnetic field $B = 0.22$T ($Ha = 100$) in *z*-direction; (d) *x-z* plane; (e) *y-z* plane; (f) growth interface

in a large solute concentration distribution non-uniformity at the solid-liquid interface. Moreover, the solute concentration distribution is 3D, a manifestation of a strong, complex, 3D flow in the liquid pool (Figure 9(c)). When the magnetic field is applied, however, the thermal convection driven by the *g*-jitter is suppressed, and consequently the solute concentration distribution becomes much more uniform both in the bulk of the liquid and at the solid-liquid interface (Figure 9(d), (e) and (f)). Detailed analysis of concentration time-evolution was performed in various planes and at many different locations. These analyses indicate that the concentration distribution does not experience a conspicuous bulk oscillation and rotation as exhibited in velocity fields (Figure 6), but the evolution of concentrations at specific locations in the liquid is oscillatory, displaying very similar behavior as shown in Figure 5.

5.4 Real g-jitter

The above study of idealized synthetic single-frequency *g*-jitter component provides a good assessment of magnetic field effects on oscillating gravity field, and helps to develop a fundamental understanding of magnetic damping in microgravity. The single frequency component, however, is far from reality in that the *g*-jitter perturbations during a typical space flight is random in nature and varies in both direction and time (Figure 1). Understanding and control of the convection generated by these random gravity signatures is of critical importance to the melt growth of consistent, high quality single crystals. In this regard, numerical simulations were carried out using the real *g*-jitter data shown in Figure 1. Here again the computations are based on the assumption that the magnetic field is switched on when the *g*-jitter sets in.

Figure 10 shows the time-evolving field variables (c, u, v and w) in the melt induced by *g*-jitter signatures with and without an applied field. It can be seen that the velocity development is random in amplitude with time and is consistent with the real *g*-jitter data in both the absence and presence of the magnetic field. Particularly noticeable is that the velocity spikes up in response to a sudden amplitude increase of the *g*-jitter perturbations, though detailed analyses show that these spikes lag behind those of the real *g*-jitter, as has been discussed in the single frequency simulations. These velocity spikes are a culprit for the irregular solute concentration distributions and defects formed in the crystals grown during the space flight. It is also clear from Figure 10 that the magnetic fields can effectively suppress the irregular convection in a real *g*-jitter environment, especially for those large amplitude velocity spikes.

The magnetic damping effects on the flow field in *x-z* and *y-z* planes at the time when the velocity spikes are shown in Figure 11. It is important to notice that without the applied field, the flow field is evidently 3D, whereas with $B = 0.22$T ($Ha = 100$), applied in the *z*-direction, the strong convection is reduced to almost a plug flow, which is qualitatively agrees with the 2D model by Shang *et al.* (2001). It is also noteworthy that with the applied field, the solute concentration spikes due to *g*-jitter induced convection are largely smoothed out as a result of substantially reduced flows (Figure 10). These results suggest that with an appropriate magnetic field, the thermal convection spikes and the solute concentration irregularities caused by *g*-jitter perturbations can be effectively reduced to below a preset threshold value required for a specific space experiment. For real *g*-jitter data, numerical simulations were also conducted with different orientations and strengths of applied magnetic fields and the

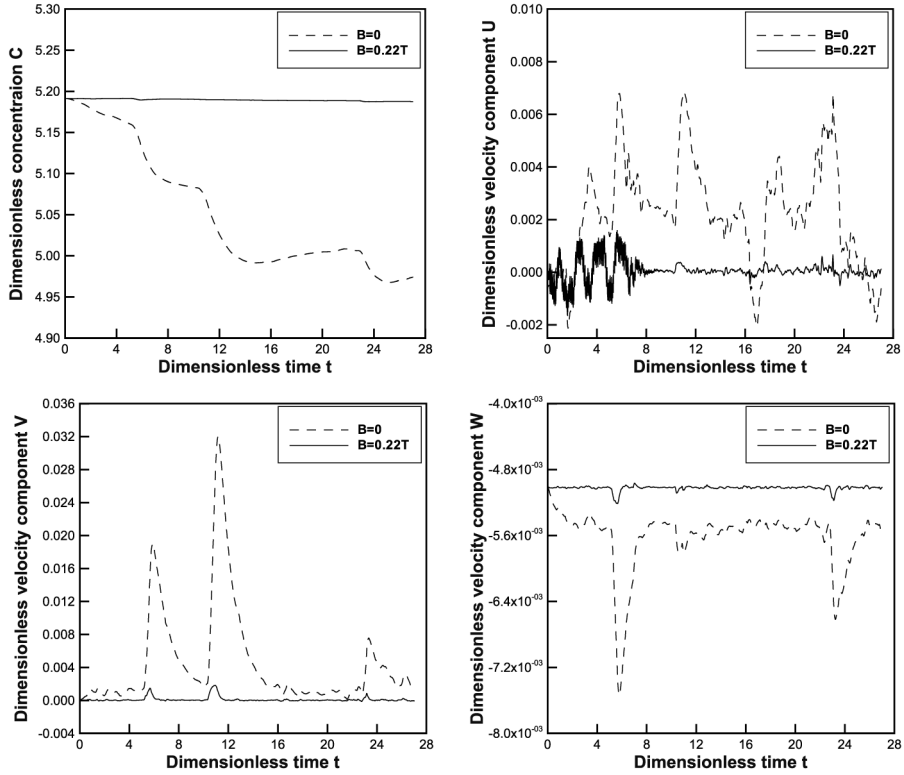

Figure 10.
Evolution of the velocity components and concentration at the location ($x = 0, y = 0, z =$ 0.1521) near the growth front under real *g*-jitter perturbations with and without applied magnetic field

conclusions are corroborated with the single frequency cases, that is, the damping is more effective with a stronger field and the field in the *z*-direction produces the strongest damping effect, in comparison with other orientations.

6. Concluding remarks

A full 3D transient finite element model has been presented for the fluid flow and heat and mass transfer phenomena in a simplified Bridgman configuration under a combined action of *g*-jitter perturbations and externally applied magnetic fields. The model is developed based on the Galerkin finite element solution of transient Navier-Stokes equations, thermal balance and solutal transport equations, and the simplified Maxwell equations. To increase the computational efficiency, an iterative procedure based on a physics-based re-numbering algorithm has been applied. Numerical simulations were conducted with steady low gravity forces, single frequency *g*-jitter and real *g*-jitter data taken during a space flight. It is found that *g*-jitter drives a complex, 3D, time dependent thermal convection even when the thermal boundary conditions are axisymmetric. During a space flight, velocity spikes emerge in response to gravity disturbances, which in turn produce irregular solute concentration distributions responsible for inconsistent crystal qualities. An

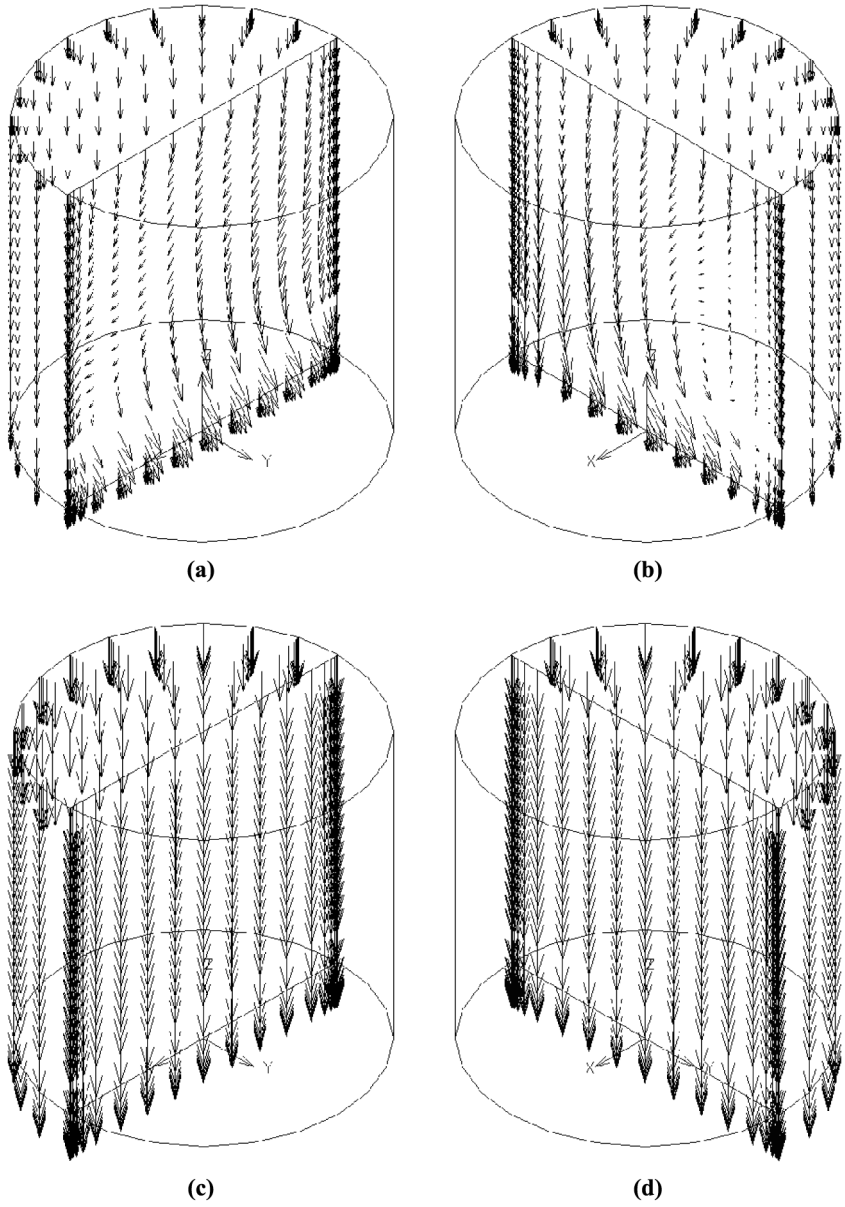

Figure 11.
The flow field patterns under the real *g*-jitter perturbations at the time related to the velocity spike in (a) *x-z* plane, $Ha = 0, U_{max} = 0.01248$; (b) *y-z* plane, $Ha = 0, U_{max} = 0.01248$; (c) *x-z* plane, $Ha = 100, U_{max} = 0.0052$; (d) *y-z* plane, $Ha = 100, U_{max} = 0.0052$

imposed magnetic field provides an effective means to suppress the deleterious effects of *g*-jitter induced convection. Simulations with external magnetic fields of various strengths and orientations show that the field aligned with the thermal gradient provides an optimal damping effect, and a stronger field is more effective

in suppressing the *g*-jitter induced convection. With or without an applied field, the convective flows and solute transport phenomena in the symmetry plane parallel to the direction of *g*-jitter are essentially 2D, for which the widely used 2D models provide a reasonably good approximation.

References

Alexander, J.I.D. and Banish, R.M. (1998), "Modeling g-sensitivity of low-gravity experiments", *Microgravity Science and Technology*, Vol. 11, pp. 90-5.

Alexander, J.I.D., Ouazzani, J. and Rosenberger, F. (1989), "Analysis of the low gravity tolerance of Bridgman-Stockbarger crystal growth. I. Steady and impulse accelerations", *Journal of Crystal Growth*, Vol. 97, pp. 21-8.

Alexander, J.I.D., Ouazzani, J. and Rosenberger, F. (1991), "Analysis of the low gravity tolerance of Bridgman-Stockbarger crystal growth. II. Transient and periodic accelerations", *Journal of Crystal Growth*, Vol. 113, pp. 21-38.

de Groh, H.C. and Nelson, E.S. (1994), "On residual acceleration during space experiments", *Proceedings of the 1994 International Mechanical Engineering Congress and Exposition HTD*, 290, pp. 23-33.

Kamotani, Y., Chao, L., Ostrach, S. and Zhang, H. (1995), "Effect of *g*-jitter on free-surface motion in a cavity", *Journal of Spacecraft and Rockets*, Vol. 32, pp. 177-83.

Li, B.Q. (1996), "*g*-jitter induced flows in a transverse magnetic field", *International Journal of Heat and Mass Transfter*, Vol. 39, pp. 2853-60.

Li, B.Q. (2001), "Stability of modulated-gravity-induced thermal convection in magnetic fields", *Physical Review E*, Vol. 63, pp. 1-9.

Li, K., Li, B.Q. and de Groh, H.C. III (2003), "Effect of magnetic field on *g*-jitter induced convection and solute striation during solidification in space", *International Journal of Heat and Mass Transfer*, Vol. 46, pp. 4799-811.

Ma, N. and Walker, J.S. (1996), "Magnetic damping of buoyant convection during semiconductor crystal growth in microgravity: spikes on residual acceleration", *Physics of Fluids*, Vol. 8, pp. 944-9.

Monti, R. and Savino, R. (1998), "G-sensitivity of microgravity experimentation – fundamental of disturbance response", *Microgravity Science and Technology*, Vol. 11, pp. 53-8.

Pan, B. and Li, B.Q. (1998), "Effect of magnetic fields on oscillating mixed convection", *International Journal of Heat and Mass Transfer*, Vol. 41, pp. 2705-10.

Series, R.W. and Hurle, D.T.J. (1991), "The use of magnetic field in semiconductor crystal growth", *Journal of Crystal Growth*, Vol. 113, pp. 305-28.

Shang, D.Y., Pan, B., Li, B.Q. and de Groh, H.C. (2001), "Magnetic damping effects on *g*-jitter driven melt convection and mass transfer in microgravity", *International Journal of Heat and Mass Transfer*, Vol. 45, pp. 125-44.

Song, S.P. and Li, B.Q. (2001), "A hybrid boundary/finite element method for simulating viscous flows and shapes of droplets in electric fields", *International Journal of Computational Fluid Dynamics*, Vol. 15, pp. 293-308.

Tang, H., Tang, Z.M., Hu, W.R., Chen, G. and Roux, B. (1996), "Numerical simulation of *g*-jitter effect on half floating zone convection under microgravity environment", *Microgravity Science and Technology*, Vol. 9, pp. 28-34.